Article

Tuning the Selectivity in the Nonoxidative Alkane Dehydrogenation Reaction by Potassium-Promoted Zeolite-Encapsulated Pt Catalysts

Published as part of JACS Au special issue "Advances in Small Molecule Activation Towards Sustainable Chemical Transformations".

Nengfeng Gong,[#] Runhui Zhou,[#] Hongliu Wan,* Huaming Hou, Xiaomeng Dou, Jianhong Gong, Peng He, and Lichen Liu*

Cite This: *JACS Au* 2024, 4, 4934−4947

Read Online

ACCESS | Metrics & More | Article Recommendations | SI Supporting Information

ABSTRACT: The significance of the nonoxidative dehydrogenation of middle-chain alkanes into corresponding alkenes is increasing in the context of the world's declining demands on transportation fuels and the growing demand for chemicals and materials. The middle-chain alkenes derived from the dehydrogenation reaction can be transformed into value-added chemicals in downstream processes. Due to the presence of multiple potential reaction sites, the reaction mechanism of the dehydrogenation of middle-chain alkanes is more complicated than that in the dehydrogenation of light alkanes, and there are few prior studies on elucidating their detailed structure−reactivity relationship. In this work, we have employed Pt catalysts encapsulated in pure-silica MFI zeolite crystallites as model catalysts and studied how the catalytic performances for dehydrogenation of *n*-pentane can be modulated by the K$^+$ promotor in the Pt-MFI catalyst. A combination of comprehensive structural characterizations by aberration-corrected electron microscopy, X-ray absorption spectroscopy, in situ CO-IR, X-ray photoelectron spectroscopy, and kinetic studies shows that K$^+$ promoter can not only influence the particle size but also modify the electronic properties of Pt species, which further affect the activity and selectivity in the dehydrogenation of *n*-pentane.

KEYWORDS: *dehydrogenation reaction, n-pentane, platinum, zeolite, metal clusters*
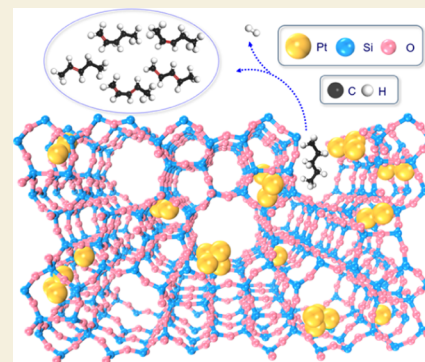
INTRODUCTION

Alkane dehydrogenation reaction is a prominent type of catalytic process in the chemical industry because it can selectively convert alkane resources into olefins, which are commodity chemicals for the polymer industry or raw materials for downstream manufacturing processes of chemicals and materials.[1] Currently, both the dehydrogenation of light alkanes (C3 and C4 alkanes) and long-chain alkanes (C10−C14 alkanes) are already practiced in commercial processes based on supported metal or metal oxide catalysts (Figure 1a,b).[2−4] However, the dehydrogenation of middle-chain alkanes (C5−C9) alkanes is much less explored in the literature, which could be related to the smaller application scope than light and long-chain alkanes in the conventional petrochemical industry.[5]

The world is transitioning from a traditional energy landscape based on fossil resources to a new energy era based on renewable resources.[6] Society's demand for transportation fuels is anticipated to decline in the next 10−20 years greatly; therefore, the major energy companies seek to develop processes for converting naphtha (made by a large portion of middle-chain alkanes) into value-added chemicals.[7] As illustrated in Figure 1c, through the dehydrogenation process, the middle-chain alkanes can be transformed into alkenes, which can be further converted

into light alkenes through the downstream cracking process.[8] The coupling of dehydrogenation and the downstream cracking process is a promising approach for the selective conversion of naphtha to light alkenes compared to the direct catalytic cracking or steam cracking process.[9]

From a mechanism point of view, the dehydrogenation of middle-chain alkanes should follow a similar reaction mechanism as the dehydrogenation of light alkanes, including the activation of C−H bonds, recombination of the H species, and the desorption of alkene products.[10−12] Nevertheless, due to the increase in the carbon chain length, the complexity of the dehydrogenation of middle-chain alkanes is substantially elevated. Various hydrocarbon products, including alkene, diene, and aromatics, can be formed, among which the alkene products will appear as a mixture of isomers (as described in Figure 1d for dehydrogenation of *n*-hexane).[13,14] In this sense, it
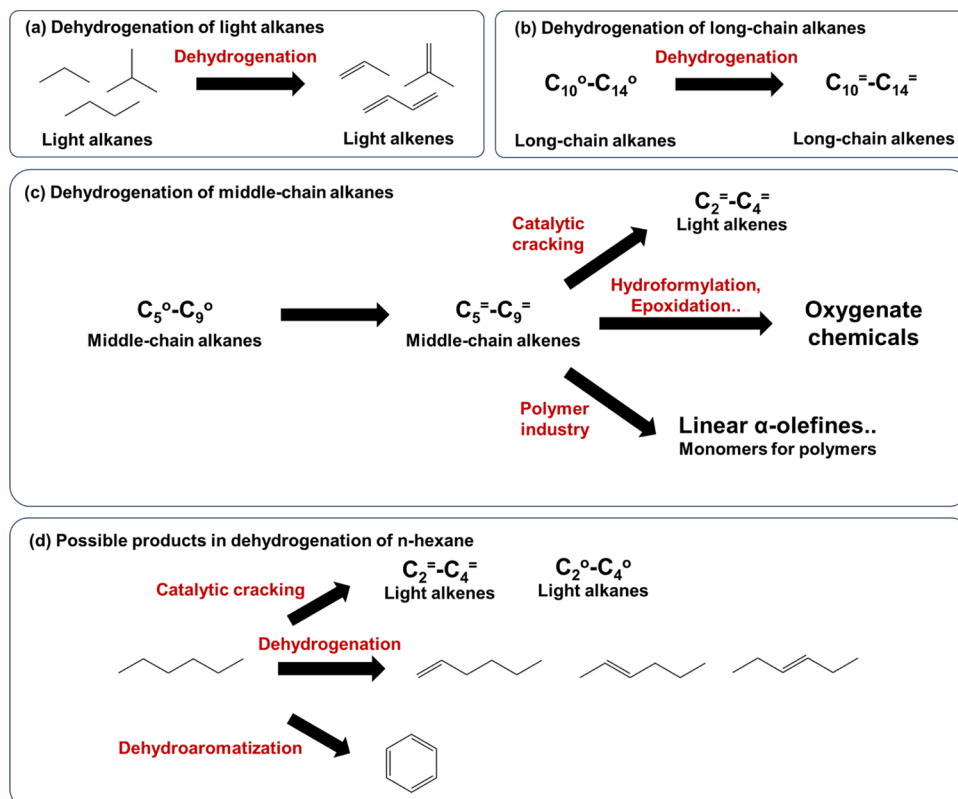
Figure 1. Dehydrogenation reactions of different types of alkanes. (a) Dehydrogenation of light alkanes to corresponding light alkenes, which are commercially available based on supported Pt or CrO_x catalysts. (b) Nonoxidative dehydrogenation of long-chain alkanes to long-chain alkenes, which are commercially available based on supported Pt catalysts. (c) Conversion of middle-chain alkanes into middle-chain alkenes through nonoxidative dehydrogenation reaction and the potential applications of the alkene products in downstream processes. (d) Possible reaction routes in nonoxidative dehydrogenation of n-hexane toward the formation of different types of hydrocarbon products.
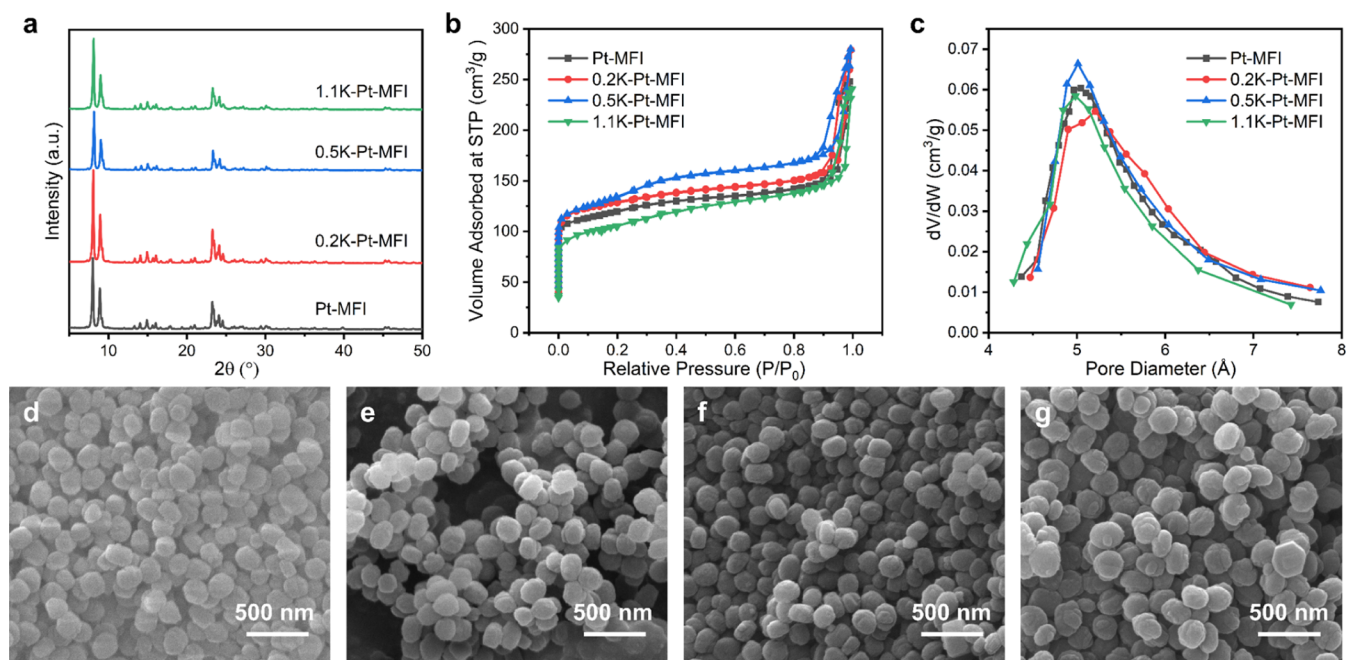
Figure 2. Characterization of metal-zeolite materials with different compositions. (a) XRD patterns of Pt-MFI catalysts with various K^+ contents. (b) N_2 adsorption and desorption isotherms. (c) Pore size distribution of xK-Pt-MFI samples. (d) SEM image of the Pt-MFI sample. (e) SEM image of the 0.2K-Pt-MFI sample. (f) SEM image of the 0.5K-Pt-MFI sample. (g) SEM image of the 1.1K-Pt-MFI sample.

is highly challenging to control the chemoselectivity and regioselectivity in the dehydrogenation of middle-chain alkanes toward a specific product. Besides, compared to the light alkenes, the tendency of coke deposition on the metal active sites
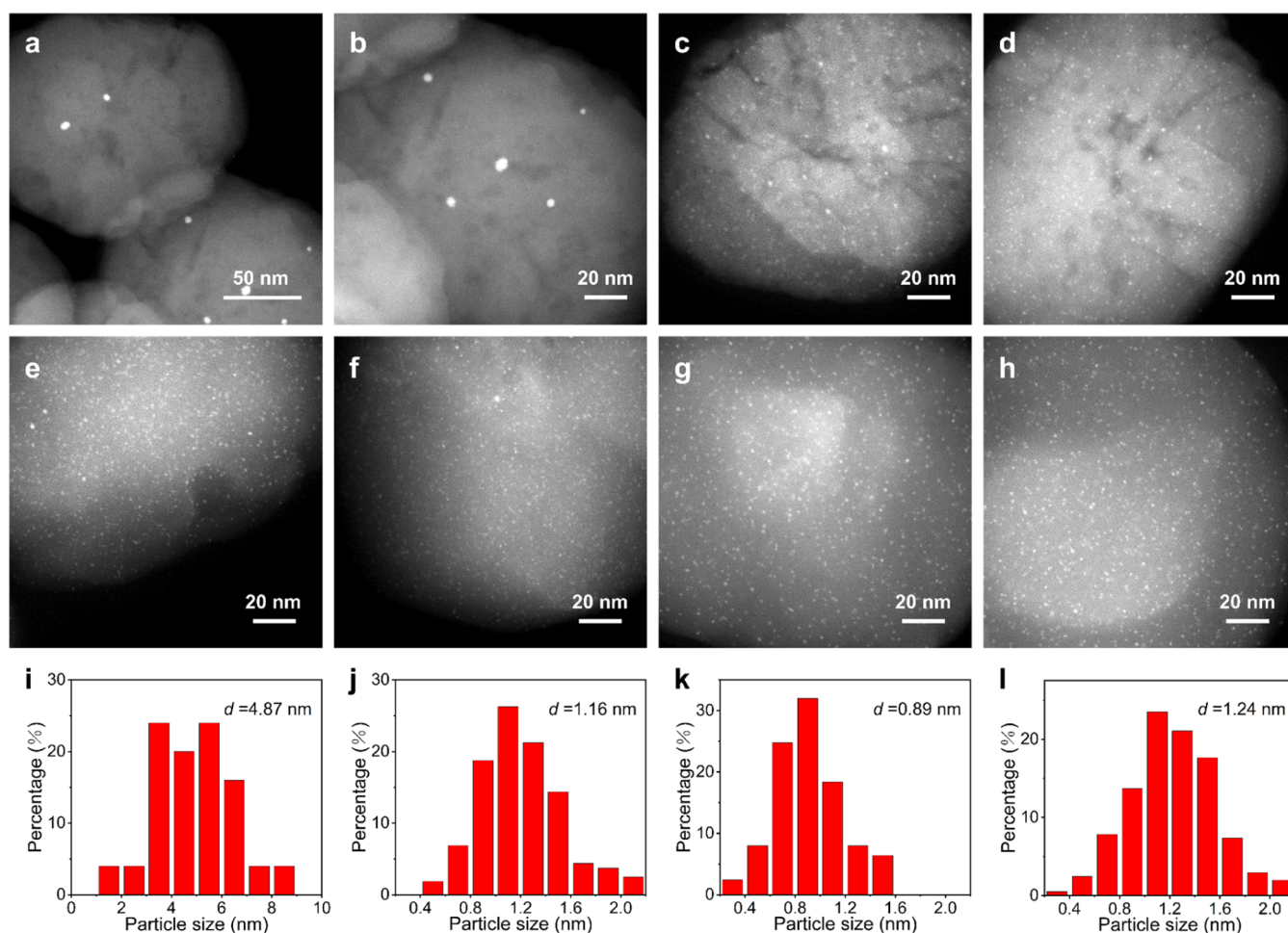
Figure 3. Structural characterization of Pt-MFI catalysts with different K contents by transmission electron microscopy. (a−h) HAADF-STEM images of the Pt-zeolite samples with different K$^+$ contents. (a, b) K-free Pt-MFI, (c, d) 0.2K-Pt-MFI, (e, f) 0.5K-Pt-MFI, and (g, h) 1.1K-Pt-MFI sample. (i−l) Size distributions of the Pt particles in different Pt-MFI samples: (i) K-free Pt-MFI, (j) 0.2K-Pt-MFI, (k) 0.5K-Pt-MFI, and (l) 1.1K-Pt-MFI. The average particle sizes of each sample were calculated by the following equation: $d = \frac{\sum n_i d_i^3}{\sum n_i d_i^2}$.

in the dehydrogenation of middle-chain alkanes could be higher due to the condensation of aromatic products. To the best of our knowledge, the relationship between the geometric and electronic structures of metal active sites and the product distributions has not yet been comprehensively revealed in previous works on supported metal catalysts.[15,16]

In this work, we employed K-promoted zeolite-encapsulated Pt catalysts as a model system to study the structure−reactivity relationship in the dehydrogenation of *n*-pentane. Based on thorough electron microscopy and spectroscopy character-izations, we have found that the geometric and electronic structures of the Pt species can be modulated by the K$^+$ promoter, which is associated with the variation of the local structures in the zeolite supports and the interactions between the Pt species and anchoring sites. By employing a series of Pt-MFI catalysts with well-characterized morphologies as model catalysts, we have concluded that the discrepancies in structural features have profound impacts on the activity, chemoselectivity, and regioselectivity in the dehydrogenation of *n*-pentane. These new insights contribute to an in-depth understanding of the role of alkali metals in stabilizing subnanometer metal sites in zeolite supports and the structure−reactivity relationship in alkane dehydrogenation reactions beyond C2−C3 alkanes by Pt-zeolite catalysts.

RESULTS AND DISCUSSION

Textual Properties of K-Promoted Pt-MFI Catalysts

The K-promoted Pt-MFI catalysts are prepared by a one-pot synthesis method, which allows the encapsulation of Pt species within the pure-silica MFI zeolite crystallites.[17] The crystal-lization conditions were kept the same for different Pt-MFI samples except for varying the K$^+$ content in the synthesis mixture (see the chemical compositions of different samples in Tables S1 and S2). It should be noted that to facilitate the diffusion of *n*-pentane molecules across the MFI zeolite crystallites, the hydrothermal crystallization of MFI zeolite is carried out at 100 °C instead of 170−180 °C in most prior works of one-pot synthesis of metal-zeolite materials to avoid the formation large zeolite crystallites. As shown in Figure 2a, regardless of the chemical composition of the K-Pt-MFI samples, all of the samples exhibit very similar diffraction patterns corresponding to typical MFI-type zeolite structures. The very similar intensities of the diffraction peaks and full width at half-maximum indicate very comparable crystallinity among different K-Pt-MFI samples. The porosity of the K-Pt-MFI samples is measured by N$_2$ adsorption isotherms and the results indicate that the micropore size distributions and pore volumes are not affected by the amount of K$^+$ promoter (Figure 2b,c and
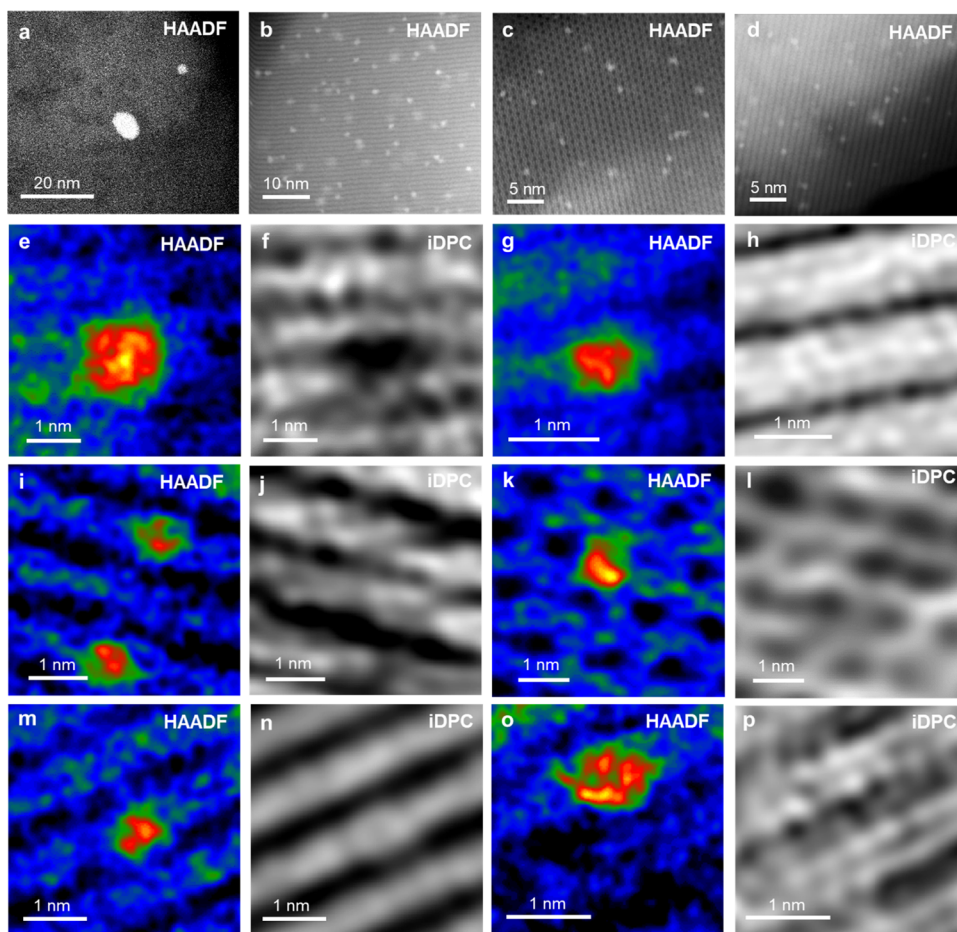
Figure 4. Characterization of Pt-zeolite samples with different K$^+$ contents by high-resolution STEM imaging technique. (a−d) Representative HAADF-STEM images at low magnifications showing the presence of subnanometer Pt clusters and small Pt nanoparticles encapsulated in MFI zeolite crystallite. (a) K-free Pt-MFI, (b) 0.2K-Pt-MFI, (c) 0.5K-Pt-MFI, and (d) 1.1K-Pt-MFI. (e−h) Paired HAADF-STEM and iDPC-STEM images showing the formation of subnanometer Pt clusters and small Pt nanoparticles in the 0.2K-Pt-MFI sample. (i−l) Paired HAADF-STEM and iDPC-STEM images showing the formation of subnanometer Pt clusters within the 10MR sinusoidal channels in the 0.5K-Pt-MFI sample. (m−p) Paired HAADF-STEM and iDPC-STEM images showing the presence of small Pt nanoparticles in the 1.1K-Pt-MFI sample.

Table S3). The very similar textual properties of various K-Pt-MFI samples are further validated by the field-emission scanning electron microscopy (FESEM) images (Figure 2d−g), which show the formation of MFI zeolite crystallites with good crystallinity and similar average crystallite sizes (150−200 nm) regardless of the K$^+$ content (Figures S1−S5).

Electron Microscopy Characterization of the K-Promoted Pt-MFI Catalysts

According to the high-angle annular dark-field scanning transmission electron microscopy (HAADF-STEM) images in Figure 3a,b, in the absence of the K$^+$ promoter, the Pt species will undergo severe sintering during the high-temperature calcination-reduction treatment after the one-pot hydrothermal synthesis. Notably, introducing a very small amount of K$^+$ promotor (ca. 0.04 wt %) can effectively stabilize the Pt species and lead to the formation of small Pt nanoparticles in the MFI zeolite (Figures S6−S7). Further increasing the K$^+$ content will cause the formation and stabilization of subnanometer Pt clusters encapsulated in MFI zeolite crystallites (Figure 3c−h). By varying the amount of K$^+$ promotor, the average particle size of the Pt species can be tuned in the range of 0.6−1.3 nm according to the histograms of the particle size distributions in Figure 3i−l. This tendency is confirmed by analysis of the size

distributions of Pt species in a variety of K-Pt-MFI samples with K$^+$ contents from 0.04 to 1.1 wt % (Figures S7−S11).

To gain further insights into the atomic-level structural features of the Pt species in the Pt-MFI samples with different K contents, we have employed the combination of high-resolution HAADF-STEM imaging technique and integrated differential phase contrast (iDPC-STEM) imaging technique for elucidating the location of Pt species within the MFI zeolite structure.[18] As shown in Figures 4a and S12, Pt nanoparticles are formed in the K-free Pt-MFI sample, some of which are embedded inside the MFI zeolite crystallites. The failure in stabilizing subnanometer Pt clusters in this sample is suggested by the absence of Pt clusters in the MFI zeolite channels in the high-resolution HAADF-STEM images. Regarding the 0.2K-Pt-MFI sample, both subnanometer Pt clusters and small Pt nanoparticles (∼1 nm) are observed in the HAADF-STEM images, which show a relatively homogeneous distribution across the zeolite crystallites (Figure 4b). The Pt nanoparticle seems to be located in a defective site within the MFI zeolite support according to the paired HAADF-STEM and iDPC images in Figure 4e,f while the Pt cluster is located in the zeolite channels (Figure 4g,h). This size-dependent preference for the location of Pt species is supported by additional paired HAADF-STEM and iDPC-STEM images (Figures S13 and S14). An increase in K$^+$
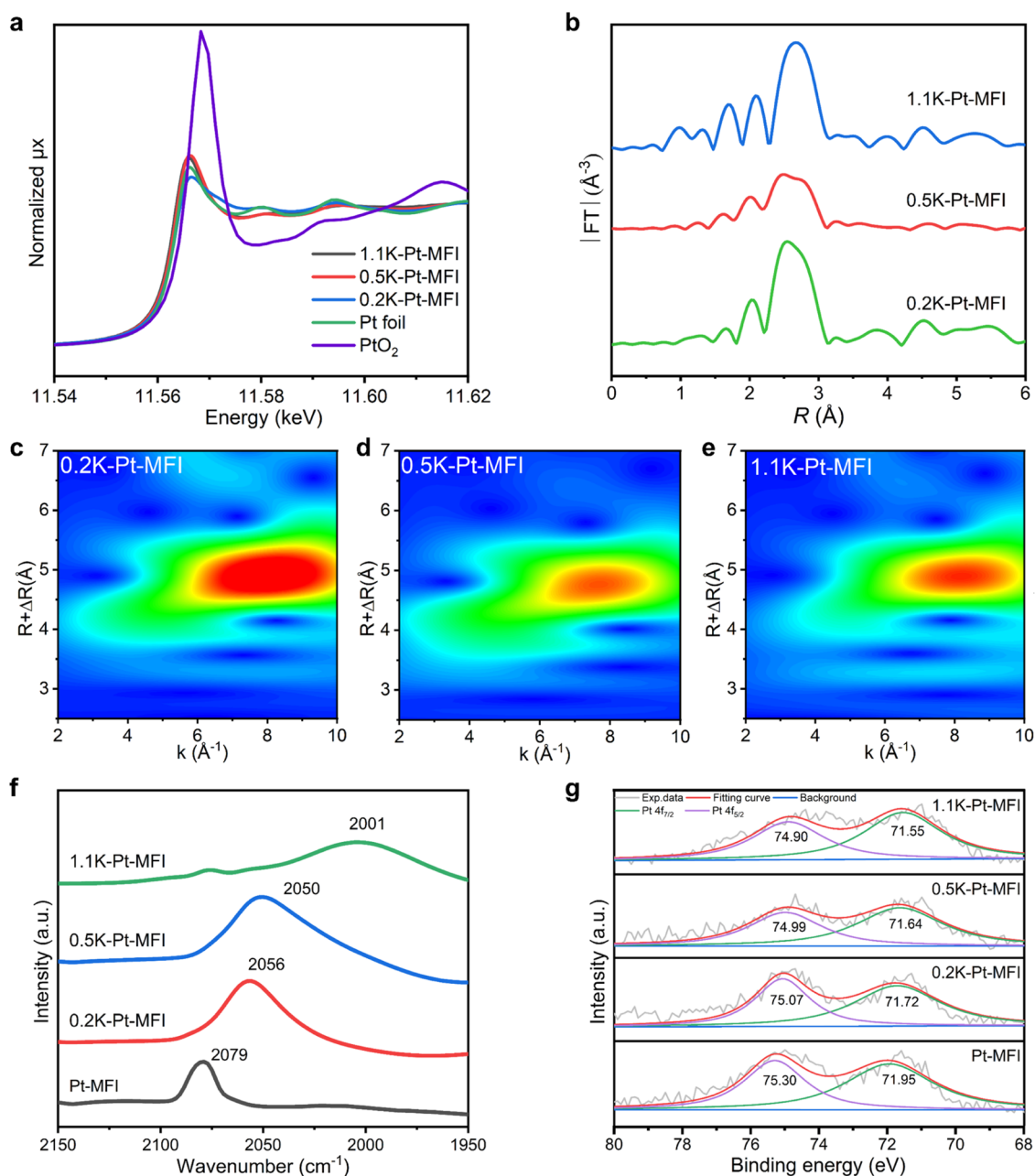
Figure 5. Spectroscopy characterizations of Pt-zeolite samples. (a) Pt L$_3$-edge XANES and (b) EXAFS spectra. (c–e) Wavelet transformation of the Pt-edge EXAFS spectra of (c) 0.2K-Pt-MFI, (d) 0.5K-Pt-MFI, and (e) 1.1K-Pt-MFI. (f) CO-IR spectra of K-Pt-MFI samples. (g) Pt 4f XPS spectra of the K-Pt-MFI samples reduced at 600 °C by H$_2$ after etching treatment by an Ar$^+$ ion beam.

content causes an improvement in the homogeneity in terms of the spatial distribution of subnanometer Pt clusters in the MFI zeolite crystallites as suggested by the HAADF-TEM images of the 0.5K-Pt-MFI sample (Figure 4c). Subnanometer Pt clusters with sizes of 0.4−0.7 nm located in the 10MR channels are observed in the paired HAADF-STEM and iDPC-STEM images (Figures 4i−l, S15, and S16). Interestingly, a further elevation of K$^+$ content causes a slight increase in Pt particle size and the formation of a higher fraction of Pt nanoparticles encapsulated in MFI zeolite crystallites in the 1.1K-Pt-MFI sample (Figure 4d) and the location of the Pt clusters and small nanoparticles are similar as the situation in the 0.2K-Pt-MFI sample (Figures 4m−p, S17, and S18). Based on the systematic electron microscopy characterizations of various Pt-MFI samples, we can conclude that, with an appropriate content of K$^+$ promotor,

subnanometer Pt clusters can be effectively stabilized in the 10MR sinusoidal channels of pure-silica MFI zeolite up to 600 °C. In the K-Pt-MFI samples with suboptimal K$^+$ contents, a fraction of Pt species will exist in the formation of small Pt nanoparticles of ∼1 nm preferentially at the defective areas within the MFI zeolite structure. These results infer that, by tuning the K$^+$ contents, we are able to tune not only the particle size but also their location in the zeolite support.

Spectroscopy Characterizations of K-Promoted Pt-MFI Catalysts

The chemical states and coordination environment of Pt species in various K-promoted Pt-MFI samples are studied by multiple spectroscopy techniques.[19−21] By in situ XAS, we have studied the chemical states of the Pt species in three typical K-Pt-MFI

samples. After reduction by H_2, all of the Pt species are in a metallic state according to the Pt L_3-edge X-ray absorption near-edge structure (XANES) spectra (Figure 5a).[20,22] In the extended X-ray absorption fine structure spectra (EXAFS) and the spectra derived from wavelet transformation, we can only observe the Pt−Pt bonding while the Pt−O contribution is not observed (Figure 5b−e).[23] The fitting results of Pt L_3-edge EXAFS spectra show that the 0.5K-Pt-MFI sample gives the lowest coordination number of first-shell Pt−Pt bonding while the 0.2K-Pt-MFI and 1.1K-Pt-MFI give higher numbers (Table 1). Besides, the coordination numbers of first-shell Pt−Pt

Table 1. Fit Results of the Pt L_3-Edge EXAFS Spectra[a]

sample	R_{Pt-Pt}	CN_{Pt-Pt}	σ^2 (Å^2)	ΔE_0 (eV)	R_{factor} (%)
0.2K-Pt-MFI	2.74(1)	8.3(5)	0.007(1)	7.0(5)	1.0
0.5K-Pt-MFI	2.72(1)	6.6(6)	0.008(1)	7.0(7)	0.3
1.1K-Pt-MFI	2.75(1)	8.7(5)	0.006(1)	7.5(9)	0.4

[a]R, bonding distance; σ^2, Debye−Waller factor; ΔE_0, inner potential correction; R_{factor}, difference between modeled and experimental data. The fits of the Pt edge were performed on the first coordination shell (ΔR = 2.0−3.0 Å) over the Fourier transform (FT) of the $k^1 k^2 k^3$-weighted $\chi(k)$ functions in the range Δk = 3.6−16.7 Å^{-1}, where Δk and ΔR are the intervals in the k and R spaces for the Fourier transformation and the fit, respectively.

bonding fit well with the average particle sizes obtained in the size histograms.[24] These results are well in line with the size distributions of Pt particles derived from the HAADF-STEM images, further validating the marked influence of the content of the K$^+$ promoter on the dispersion of Pt on MFI zeolite.

Considering that the discrepancies in electronic properties of Pt species can be better probed by CO-IR (IR spectroscopy using CO as probe molecule) technique,[25,26] we have conducted the in situ CO-IR measurements on typical Pt-MFI samples. As shown in Figure 5f, in the K-free Pt-MFI sample, we can observe the adsorption of CO on Pt nanoparticles in the linear configuration.[19,25,27,28] With the increase of K$^+$ content to 0.2 and 0.5 wt %, shifts in the CO adsorption bands toward the lower wavenumbers are observed and ascribed to the rise of under-coordinated Pt sites with the K$^+$ content. Interestingly, in the case of the 1.1K-Pt-MFI sample, we observe a broad CO adsorption band at 2050−1950 cm^{-1}, which could be associated with electron-rich Pt sites.[29,30]

The electronic features of the Pt species are also studied by quasi in situ XPS, in which the Pt-MFI samples were reduced by H_2 and then directly transferred to the analysis chamber without exposure to air.[31,32] Moreover, we performed an Ar$^+$ etching treatment to remove part of the surface zeolite structure to detect the encapsulated Pt species within the MFI crystallites. As shown in Figure 5g, we can see the shift of the Pt 4f region toward lower binding energies as the increase of K$^+$ content. In particular, a binding energy shift of ∼0.4 eV is observed between the K-free Pt-MFI and the 1.1K-Pt-MFI sample in the Pt 4f region acquired after Ar$^+$ etching treatment. Together with the CO-IR results, we can conclude that adding K$^+$ favors the formation of electron-rich Pt species within the MFI zeolite structure.[21]

Based on prior studies, the subnanometer Pt clusters/nanoparticles are probably located at the sites with a local defect (e.g., the silanol nests) within the MFI zeolite channels.[33] The presence of excess K$^+$ will cause the formation of abundant ≡Si−O$^−$−K$^+$ sites during the one-pot synthesis process, and the

electron transfer from these sites to Pt clusters/nanoparticles may cause the formation of electron-rich Pt species in the 1.1K-Pt-MFI sample. This speculation is in line with the literature studies on the electronic properties of Pt species in conventional supported Pt catalysts promoted by alkaline metals.[34,35] We would like to note that the observation of the CO adsorption band on Pt sites at ∼2000 cm^{-1} and the substantial binding energy shift by XPS infer a higher level of electron transfer from the support to the Pt sites, resulting in the formation of electron-rich Pt species with a higher level of negative charge in the 1.1K-Pt-MFI sample than those formed on conventional solid carriers (e.g., SiO$_2$, Al$_2$O$_3$, TiO$_2$, etc.).[36,37] The formation of electron-rich Pt species promoted by K$^+$ is also inferred by the shift of the Pt L_3-edge XANES spectra (Figure S19). The favored formation of electron-rich Pt species in the 1.1K-Pt-MFI sample could be associated with the unique structures of the Pt clusters surrounding by the MFI zeolite framework and the Pt-zeolite interfaces in the confined space formed through the bonding between Pt clusters and the ≡Si−O$^−$−K$^+$ sites.

Understanding the Influence of K$^{\pm}$ Promotor

According to the structural characterizations of a series of K-Pt-MFI catalysts, it is valid that the amount of K promoter can substantially impact the dispersion of Pt species within the pure-silica MFI zeolite. Considering the broad applications of alkaline promotors in the synthesis of metal-zeolite catalysts, it is of interest to elaborate the mechanism of alkaline promotors in stabilizing metal species within the zeolite structure. The electron microscopy images of the Pt-zeolite materials derived from different stages of the one-pot synthesis procedure show that, in the as-synthesized Pt-zeolite samples obtained after the hydrothermal synthesis, Pt should exist in the form of atomically dispersed species within the MFI zeolite crystallites, regardless of the K$^+$ content in the samples (see Figures S20−S23). After the calcination treatment in air for the removal of ligands and organic structure-directing agents, distinct morphologies are observed with different K-Pt-MFI-air samples. As shown in Figure S24, without the K$^+$ promotor, severe sintering of Pt species into large Pt particles is observed in the K-free Pt-MFI-air sample, because the oxidized Pt species (PtO$_x$) are volatile and migrate out of the zeolite crystallites through the microporous channels during calcination and then form large Pt particles on the external surface of MFI zeolite crystallites. The uncontrollable sintering of the Pt species originates from the weak interaction between the PtO$_x$ species and the zeolite framework (or the silanol groups within the zeolite structure).

In the K-containing Pt-MFI-air samples, the formation of Pt nanoparticles is greatly suppressed (Figures S25−S28). Especially, in the 0.5K-Pt-MFI-air sample, the Pt species seem to exist as atomically dispersed Pt and very tiny Pt clusters (<0.4 nm) (Figure S26). However, introducing excess K$^+$ will cause the formation of a small fraction of Pt clusters in the 1.1K-Pt-MFI-air sample, implying the detrimental impacts of excess K$^+$ in the synthesis mixture of Pt-MFI materials. Despite the minor differences in the size distributions of Pt species, the formation of Pt particles of >3 nm during the high-temperature calcination procedure is inhibited by the K$^+$ promotor. Consequently, considerable portions of Pt species can be stabilized as Pt clusters and small nanoparticles of ∼1 nm in the reduced K-Pt-MFI samples. By monitoring the morphological evolution of Pt-zeolite materials along the materials synthesis procedure, we can conclude that mitigating the uncontrollable sintering of Pt species during the exothermic calcination process is more critical
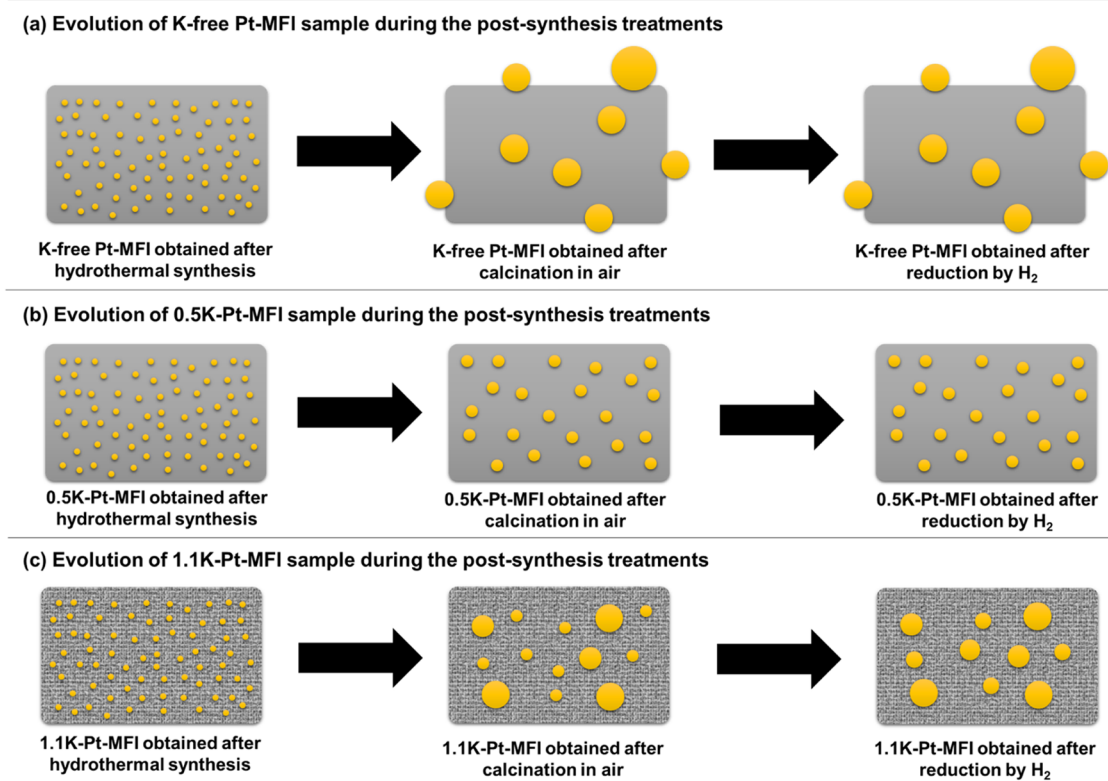
Figure 6. Structural evolution of Pt-zeolite materials with different K contents during the postsynthesis treatments. (a) K-free Pt-MFI, (b) 0.5K-Pt-MFI, and (c) 1.1K-Pt-MFI. In the case of K-free MFI and 0.5K-Pt-MFI, the zeolite supports have higher structural integrity than the 1.1K-Pt-MFI sample because the latter one contains a large number of defects in the zeolite framework.

than the H_2 reduction process because the PtO_x species have much higher mobility than the reduced Pt species on the zeolite support.

Combining the electron microscopy characterization results of Pt-MFI materials at different synthesis stages, we attempt to clarify the role of K^+ in stabilizing subnanometer Pt clusters in MFI zeolite. As illustrated in Figure 6, the influence of K^+ is mostly reflected in the calcination step in which the K^+ can protect the Pt species from agglomeration during the high-temperature calcination process. By IR spectroscopy (Figure S28), we have confirmed that the introduction of K^+ can effectively neutralize the silanol groups in the MFI zeolite, and the resultant $\equiv Si-O^- -K^+$ species can serve as the anchoring sites for the mobile PtO_x species generated during the high-temperature calcination process because the PtO_x species can be better stabilized by the electron-rich O species in the $\equiv Si-O^- -K^+$ sites than that in the $Si-OH$ groups.[38] Consequently, the dispersion of Pt species can be maintained after high-temperature treatments in K-containing Pt-MFI materials.

To effectively stabilize the Pt species, a sufficient content of K^+ is required, which can explain the higher dispersion of Pt species in the 0.5K-Pt-MFI sample than in the 0.2K-Pt-MFI sample. As the K^+ content is further elevated to 1.1 wt %, the crystallization of MFI zeolite is affected, as indicated by the observation of abundant mesopores in the HAADF-STEM images (Figure S27). The presence of a higher number of defective sites induced by the excess K^+ is also inferred by the IR spectra, in which several IR bands associated with silanol nests are observed with the 1.1K-Pt-MFI sample, while these bands are hardly observed in the 0.5K-Pt-MFI sample. The lower degree of structural integrity of the 1.1K-Pt-MFI sample is also reflected in the ^{29}Si

solid-state NMR spectra, in which we can see a higher ratio of Q3/Q4 in 1.1K-Pt-MFI than 0.5K-Pt-MFI sample (Figure S29).[39,40] The observation of more defective sites in the 1.1K-Pt-MFI sample could be associated with the influence of K^+ on the crystallization process of MFI zeolite.[41,42] The presence of mesoporous defects in the MFI zeolite crystallites is detrimental to the stabilization of subnanometer Pt species during the high-temperature post-synthesis treatments, resulting in the growth of Pt particles and a lower dispersion of Pt species in the 1.1K-Pt-MFI sample compared to the 0.5K-Pt-MFI sample.

Though numerous studies have shown the marked impacts of alkaline promoters on zeolite-supported noble metal catalysts for various reactions, there is still a lack of in-depth understanding of the working mechanism of alkaline metals in modifying the particle size, electronic properties, and spatial distribution of noble metal species within the zeolite matrices.[43–45] The above results infer that a unified understanding of these issues can be achieved by elaborating the influence of alkaline metals on the abundance and chemical nature of the anchoring sites for the noble metal species. Future works toward a more accurate elucidation of the working mechanism might be reached by combining the experimental characterizations of the coordination environment of metal species at the anchoring sites and theoretical modeling of the plausible configurations in different atmospheres.[46–48]

Catalytic Results for Pentane Dehydrogenation Reaction

The catalytic properties of K-promoted Pt-MFI catalysts comprising different types of Pt species for the dehydrogenation of middle-chain alkanes are performed in a fixed-bed reactor at atmospheric pressure by employing *n*-pentane as the model reactant. Initially, the catalytic tests are performed with a
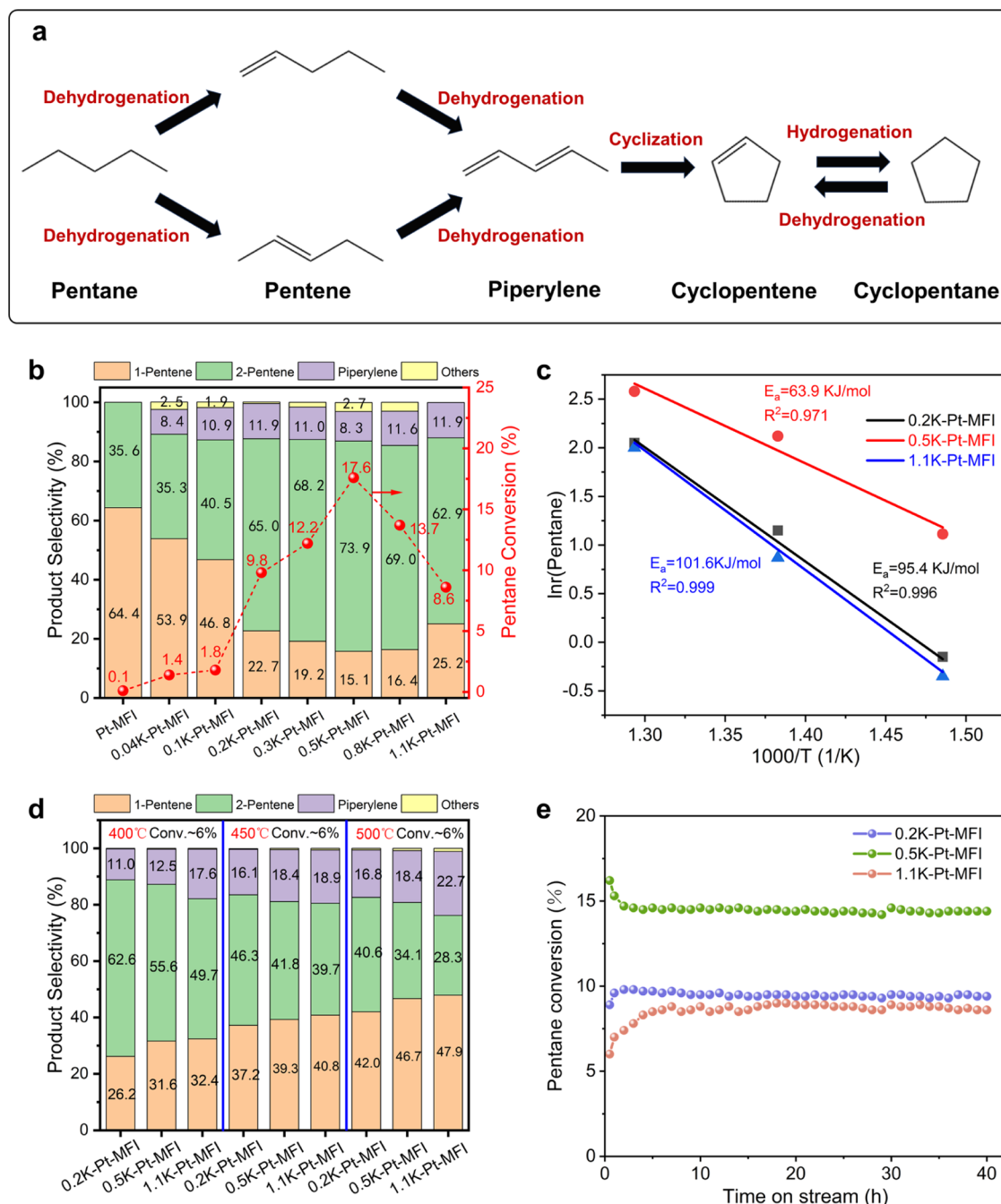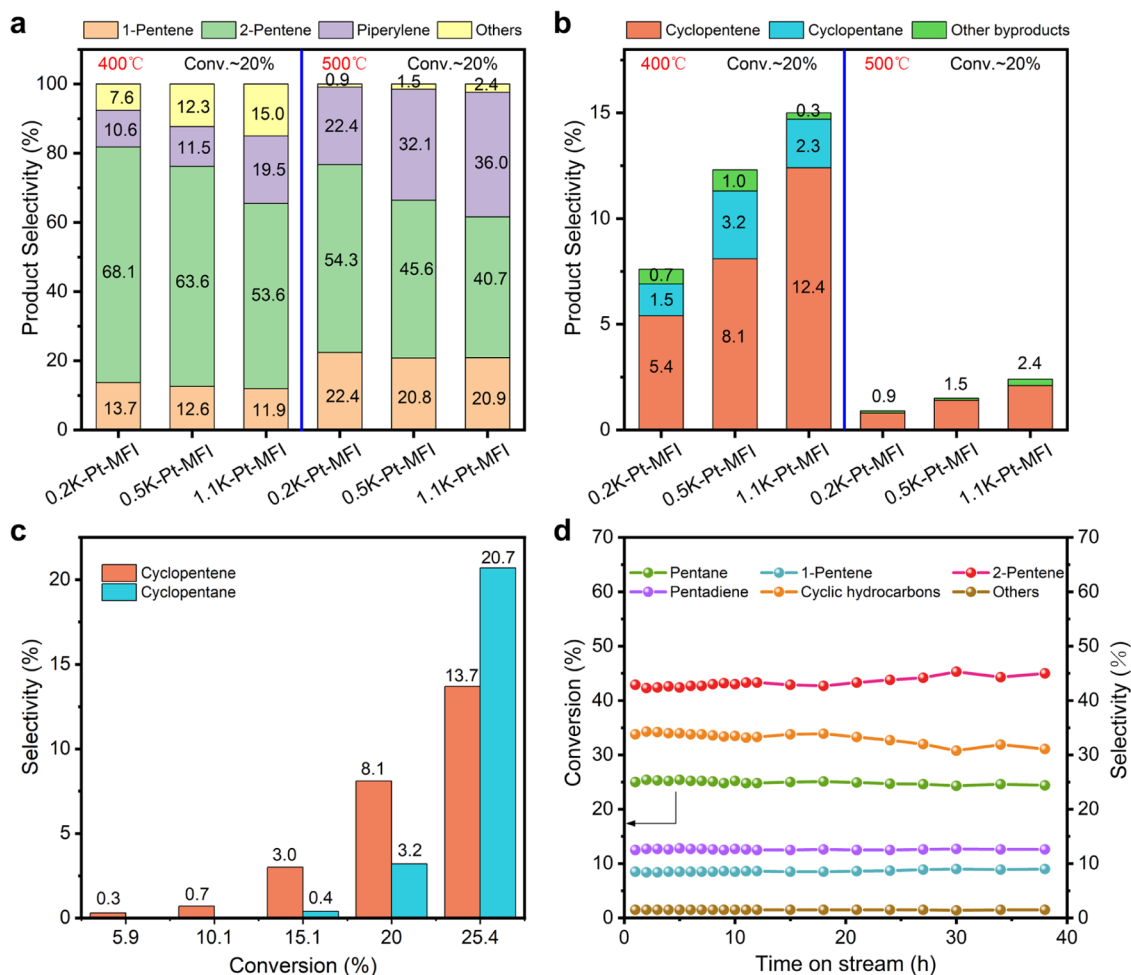
Figure 7. Catalytic tests of metal-zeolite catalysts for pentane dehydrogenation. (a) Reaction pathways of pentane dehydrogenation over K-Pt-MFI catalysts. (b) Initial specific activities of K-Pt-MFI with different K contents for pentane dehydrogenation. Reaction conditions: 400 °C, 100 mg of catalyst diluted with quartz sand in a 1:4 mass ratio, 25 kPa of pentane balanced with N_2, WHSV = 29.2 h^{-1}. (c) Arrhenius plots characterizing pentane dehydrogenation and the corresponding activation energies of K-Pt-MFI samples. (d) Product distribution of different metal-zeolite catalysts calculated based on pentane under low conversion condition at 400, 450, and 500 °C. (e) Stability test of the K-Pt-MFI catalysts for the pentane dehydrogenation reaction. Reaction conditions: 400 °C, 100 mg catalyst diluted with quartz sand in a 1:4 mass ratio, 25 kPa of pentane balanced with N_2, WHSV = 29.2 h^{-1}.

relatively high weight hour space velocity (WHSV) to differentiate different Pt-zeolite catalysts. As shown in Figure 7a, the activities for the *n*-pentane dehydrogenation reaction of the Pt-MFI catalysts are greatly dependent on the content of the K promotor. The K-free Pt-MFI sample gives negligible conversion of *n*-pentane, and introducing a small amount of K⁺ (0.04−0.1 wt %) into the Pt-MFI catalyst can improve the activity, resulting in a detectable conversion of *n*-pentane to pentenes (mixture of 1-pentene and 2-pentene) and a small

portion of piperylene. Further increasing the K⁺ content to 0.2 wt % will cause a substantial increase in the *n*-pentane conversion to 9.8%. When the K⁺ content is elevated to 0.5 wt %, the resultant 0.5K-Pt-MFI catalyst exhibits the highest pentane conversion among the tested samples and further increasing the K⁺ content to 0.8 and 1.1 wt % will cause the drop of catalytic activity. Besides the significant influence of the K⁺ content on the activity, product distributions are also greatly dependent on the K⁺ content. A clear tendency in the variation

Figure 8. Catalytic tests of metal-zeolite catalysts for pentane dehydrocyclization. (a, b) Product distribution of different metal-zeolite catalysts calculated based on pentane under high conversion condition at 400 and 500 °C. The inset shows the selectivity of cyclopentane and cyclopentene enlarged from the left image. (c) Initial selectivity of cyclopentane and cyclopentene over 0.5K-Pt-MFI catalyst at different pentane conversion. (d) Stability test of the 0.5K-Pt-MFI catalysts for the pentane dehydrogenation reaction. Reaction conditions: 400 °C; atmospheric pressure; pentane partial pressure: 25 kPa; WHSV = 1.6 h^{-1}.

of the selectivity to 2-pentene (including the *cis*-2-pentene and *trans*-2-pentene) is reflected in Figure 7a, which indicates a positive correlation between the pentane conversion and the selectivity to 2-pentene. In terms of the selectivity to piperylene, it varies in a much lower degree of amplitude because all of the K-containing Pt-MFI samples give a selectivity to piperylene of ~10%.

Moreover, we have conducted catalytic tests in the kinetic regime to gain insights into the intrinsic activities of the Pt sites in various K-Pt-MFI samples at 400−500 °C.[49] As shown in Figure 7b, the apparent activation energies derived from the Arrhenius plots show that the 0.2K-Pt-MFI and 1.1K-Pt-MFI samples give similar activation energies for pentane dehydrogenation reaction, while the 0.5K-Pt-MFI sample gives a considerably lower activation energy. By normalizing the reaction rates on exposed surface Pt sites measured by CO chemisorption, we can quantify the intrinsic activities of Pt sites in different K-Pt-MFI samples. As shown in Figure S30, the Pt sites in the 0.5K-Pt-MFI sample show 30−40% higher turnover frequency than the Pt sites in the 0.2K-Pt-MFI and 1.1K-Pt-MFI samples. These results are consistent with the performance data presented in Figure 7a, inferring that the K+ promoter can

remarkably modify the capability of Pt sites to activate pentane molecules.

We further examined the product distributions of the *n*-pentane dehydrogenation reaction at different temperatures. As displayed in Figure 7c, at very close conversion levels of pentane (~6%) achieved by tuning the WHSV at 400 °C, we can observe considerable differences in the product distributions among three representative K-Pt-MFI catalysts. For the 0.2K-Pt-MFI sample, 2-pentenes appear as the predominant product (62.6%) followed by the contribution of 1-pentene (26.2%) and piperylene (11.0%). With the stepwise increase of K content to 0.5 and 1.1 wt %, the portion of 2-pentenes decreases to 55.6 and 49.7%, respectively. Notably, the selectivity to piperylene increases to 17.6% with the 1.1K-Pt-MFI catalyst, accompanied by an increase of selectivity to 1-pentene (32.4%). The marked influences of K+ content on the product distributions are also reflected in the catalytic results obtained at 450 and 500 °C and the variation tendencies of the three major products are quite similar to those observed at 400 °C. Elevating the reaction temperature will cause a marked increase in selectivity to piperylene and 1-pentene and a decrease in selectivity to 2-pentene. Because the conversions of *n*-pentane are maintained at low levels (~6%) in the tests, the discrepancies in production

distributions should be caused by the structural features of the active sites rather than the thermodynamic equilibria of different compounds in the reaction mixtures. Based on the product distributions shown in Figure 7a−c, we can conclude that dehydrogenation of *n*-pentane on a supported Pt catalyst is a structure-sensitive reaction and one can modulate the selectivity to a target product (1-pentene, 2-pentene, or piperylene) by tuning the K^+ content and the reaction temperature.

Dehydrocyclization of *n*-Pentane

As illustrated in Figure 7a, besides the linear alkene products, *n*-pentane can also be converted into cyclic hydrocarbons (cyclopentane and cyclopentene) through a dehydrocyclization reaction. Indeed, when the *n*-pentane dehydrogenation reaction was performed with the K-Pt-MFI catalyst at 400 °C at a low WHSV, we could observe a substantial amount of cyclic hydrocarbons in the products (Figure 8a). The selectivity for cyclic hydrocarbons increases with the K^+ content in the K-Pt-MFI catalyst. When the *n*-pentane conversion levels are kept at ~20%, the 1.1K-Pt-MFI catalyst can achieve a total selectivity of ~15% to cyclopentane and cyclopentene. Though the 0.5K-Pt-MFI sample gives a slightly lower total selectivity to cyclic hydrocarbons (12.3%), its much higher intrinsic activity for activating C−H bonds enables the achievement of a higher space-time yields of cyclic hydrocarbons than the 1.1K-Pt-MFI catalyst. From a thermodynamic point of view, the dehydrocyclization reaction is more favorable at relatively low temperatures, as implied by the low selectivities for cyclic products at 500 °C with the K-Pt-MFI catalysts (Figure 8a). Our optimization experiments with the 0.5K-Pt-MFI catalyst at 400 °C and different WHSV show that at ~25% conversion of *n*-pentane, the total selectivity to cyclopentane and cyclopentene can reach ~35% (Figure 8b,c). To the best of our knowledge, this is the highest selectivity achieved through a nonoxidative dehydrogenation process in a fix-bed reactor.

According to the literature study of the reaction mechanism of dehydrocyclization of *n*-hexane, the formation of cyclopentene could be produced through the cyclization of piperylene, which can be further converted to cyclopentane due to the hydrogenation reaction. This speculation is implied by the high selectivity achieved with the 1.1K-Pt-MFI catalyst because this catalyst favors the production of piperylene over other catalysts. Moreover, the yields of cyclic hydrocarbons increase dramatically with the conversion of *n*-pentane, suggesting that piperylene could be the intermediate for the dehydrocyclization reaction. Regarding the active site for the dehydrocyclization step, we think it is a synergy between the Pt sites (responsible for the C−H activation toward the formation of alkenes) and the weak acid sites in the MFI zeolite support (such as the residual −OH groups, which are responsible for the cyclization reaction).[50] Considering the broad applications of cyclopentane as a blowing agent in the manufacturing of polyurethane and an eco-friendly refrigerant and the great potential of cyclopentene as the precursor of degradable polymers, the dehydrocyclization of *n*-pentane can be a promising route for converting the excess pentane resource into value-added chemicals and materials.[51] We anticipate that, by further optimizing the composition of the zeolite framework and the chemical composition of the Pt active sites, the efficiency in converting *n*-pentane into cyclic hydrocarbons can be further improved, which may pave a new way for manufacturing C5-based chemicals and materials based on bifunctional zeolite-supported Pt catalysts.[22,52]

Structure−Reactivity Relationship

The above catalytic results have demonstrated the profound impacts of the K^+ promoter on the catalytic performances of Pt-MFI catalysts for the *n*-pentane dehydrogenation reaction. Prior experimental and theoretical studies on the propane dehydrogenation reaction have shown that the activation of C−H bonds is normally the rate-determining step for dehydrogenation of light alkanes (C2−C4 alkanes) and the cleavage of C−H bond is favored on under-coordinated Pt sites than on highly coordinated Pt sites.[46,53,54] We have carried out an isotopic study to measure the H−D exchange rates of D_2 and C_2H_6 on different Pt-zeolite catalysts and found that the capability for H−D exchange is well correlated with their activity for pentane dehydrogenation reaction (Figure S31), implying that the activation of C−H bonds is indeed to be a critical step for *n*-pentane dehydrogenation reaction.[55]

The structural characterizations of a series of K-Pt-MFI samples show that when varying the K^+ content, both the geometric structures (reflected by the particle size distributions) and electronic structures (reflected by XPS and CO-IR data) of the Pt sites encapsulated in MFI zeolite are modulated, leading to the difficulty in determining the impact weight of each factor in the *n*-pentane dehydrogenation reaction. By comparing the product distributions of the 0.2K-Pt-MFI and 1.1K-Pt-MFI samples with similar average Pt particle sizes, the production of piperylene is favored with the sample with a higher K^+ content, although the two samples exhibit similar activities and apparent activation energies for the *n*-pentane dehydrogenation reaction. Considering the large discrepancies in the electronic properties of Pt species in these two samples, the negatively charged Pt species should be responsible for the high selectivity to piperylene.

From a mechanistic point of view, the formation of piperylene results from the further dehydrogenation of 1-pentene or 2-pentene on Pt sites through the cleavage of C−H bonds in these molecules. Although the 0.5K-Pt-MFI sample delivers the highest specific activity in the first-step dehydrogenation reaction, the formation of the second C═C bond is more favorable in the 1.1K-Pt-MFI sample. The electron-rich Pt species with large particle sizes in the 1.1K-Pt-MFI may facilitate the adsorption of the primary pentene molecules according to the temperature-programmed desorption profiles of 1-butene on the K-Pt-MFI samples (Figure S32) and stabilization of the intermediates in the dehydrogenation of pentene toward the formation of piperylene. The difference in particle size can also cause the different 2-pentene/1-pentene ratios among the K-Pt-MFI samples because the isomerization transformation between the pentenes is sensitive to the atomic arrangements on the Pt surface, which is associated with the particle size.[56,57]

Stability Tests of K-Pt-MFI Catalyst for *n*-Pentane Dehydrogenation

For supported metal catalysts used in dehydrogenation reactions of light alkanes (e.g., ethane and propane), the metal active sites inevitably suffer coke deposition under reaction conditions, leading to catalyst deactivation. To address the potential stability issue, we have monitored the 0.2K-Pt-MFI, 0.5K-Pt-MFI, and 1.1K-Pt-MFI samples under high WHSV conditions at 400 °C (Figure 7d), which in principle is a preferred condition for detecting the catalyst's deactivation behavior. During the testing periods (~40 h), both catalysts show negligible deactivation, suggesting their high stability against deactivation under the tested conditions. The robustness of the Pt particles

encapsulated in the MFI zeolite crystallites is further confirmed by the HAADF-STEM images of the spent catalysts (Figures S33–S35). The perseverance of the location of the subnanometer Pt clusters is also confirmed by the paired HAADF-STEM and iDPC-STEM images (Figure S36). The alleviated deactivation could be associated with a much lower reaction temperature than those for dehydrogenation of light alkanes (550–650 °C).[22,55] When the reaction temperature is elevated to 500 °C, the initial conversion of *n*-pentane increases to ∼40% with a ∼50% selectivity to 1-pentene and 2-pentene as well as ∼35% selectivity to piperylene (Figure S37). Notably, we observe a gradual deactivation of the 0.5K-Pt-MFI catalyst during the time on stream, which should be caused by coke deposition at the active sites according to the characterizations of the spent catalyst by EDS mapping, Raman spectroscopy, and thermogravimetric analysis (Figures S38–S40). Notably, the size distribution of the Pt particles almost remained unchanged after the dehydrogenation test at 500 °C (Figure S41). In this sense, in light of the prior works of Pt-zeolite catalysts for the dehydrogenation of light alkanes, introducing a cocatalyst metal (e.g., Sn, In, Zn, etc.) would be an alternative solution for mitigating the rapid deactivation issue at high reaction temperatures, which will be explored in our future study.[22,46]

The stability test at 400 °C with a relatively low WHSV confirms the high durability of the 0.5K-Pt-MFI catalyst for producing cyclic hydrocarbon products (Figure 8d). The conversion of *n*-pentane remains at ∼25% during the testing period (∼40 h) and the selectivity to cyclic hydrocarbons maintains >30%, suggesting that the 0.5K-Pt-MFI catalyst is a promising candidate for dehydrocyclization of *n*-pentane.

◼ CONCLUSIONS

In this work, we have shown the preparation and structural characterizations of K-Pt-MFI catalysts and elucidated the structure–reactivity relationships for nonoxidative dehydrogenation of *n*-pentane. Both the geometric structures (i.e., particle size) and electronic structures of Pt species can be modulated by the alkaline promotor (i.e., K$^+$), which further affects their performances in the dehydrogenation of *n*-pentane. The insights presented in this study can be further translated into other zeolite-encapsulated metal catalysts for understanding the role of alkaline metals in stabilizing subnanometer metal sites in zeolite structure and the catalytic consequences for activation of C–H bonds in hydrocarbon molecules and control of the product distributions toward multiple hydrocarbon products as a strategy for sustainable utilization of naphtha resources.

◼ EXPERIMENTS

Materials Synthesis

Synthesis of the Pt-MFI Catalyst. Pt nanoparticles encapsulated in purely siliceous MFI zeolite were prepared by a one-pot synthesis method. First, the solution of the organic structure-directing agent was prepared by mixing 20.1 g of deionized water and 8.12 g of tetrapropylammonium hydroxide (TPAOH) solution (40 wt %, K-free, Alfa-Aesar, product code: 17456.22) in a beaker at room temperature. Then, 8.24 g of tetraethyl orthosilicate (TEOS, Alfa-Aesar, >99%) was added to the mixed solution and stirred at 300 rpm for 6 h. Subsequently, 300 μL of H$_2$PtCl$_6$ (Sigma-Aldrich, >99.9%) aqueous solution (0.25 mol·L^{-1}) and 300 μL of ethylenediamine (Sigma-Aldrich, >99.9%) were added successively to the resultant solution and stirred at room temperature for 5 min. The resulting yellow solution was then divided into two equal parts and transferred to two 50 mL Teflon-lined autoclaves, which were then heated in an electric oven at 100 °C for 24 h. After the hydrothermal reaction, the

white solid products were isolated by centrifugation and washed twice with deionized water and ethanol. Finally, the solid product was dried at 60 °C for 12 h and calcined in air at 560 °C for 8 h and 600 °C for 2 h. The obtained sample was termed Pt-MFI.

Synthesis of the K-Promoted Pt-MFI Catalyst. The K-promoted Pt-MFI catalysts were prepared by a procedure similar to that for Pt-MFI catalyst, with the exception that K-containing TPAOH (20 wt %, containing ∼0.6 wt % of K, Sigma-Aldrich, product code: 254533-100G) was used. The K-containing TPAOH solution was prepared by mixing TPAOH (40 wt %, K-free, Alfa-Aesar, product code: 17456.22), TPAOH (20 wt %, containing ∼0.6 wt % of K, Sigma-Aldrich, product code: 254533-100G), and deionized water in a beaker at room temperature. The specific combinations of TPAOH (Sigma-Aldrich), TPAOH (Alfa-Aesar), and deionized water are summarized in Table S1.

Characterization

The chemical compositions of the catalyst samples were determined by inductively coupled plasma optical emission spectrometry (ICP-OES) with an Optima 2100DV instrument manufactured by PerkinElmer.

X-ray diffraction patterns (XRD) of the prepared samples were obtained using a Bruker D8 advanced X-ray diffractometer with Cu Kα radiation ($\lambda = 0.15418$ nm) over a 2θ range of 5–50° with a scan rate of 0.04°/s.

Scanning electron microscopy (SEM) was used to analyze the crystalline morphology and size of the zeolite particles, processed on an FEI QUANTA 400F scanning electron microscope at 10 kV. Additionally, the distribution of Pt clusters was determined by transmission electron microscopy (TEM) and high-angle annular dark-field scanning transmission electron microscopy (HAADF-STEM) on a JEOL-2100F microscope at 200 kV and Cs-corrected FEI Titan Themis operating at 300 kV. The powder samples were suspended in CH$_2$Cl$_2$ and ultrasonicated for 15 min, then dropped onto carbon-coated copper grids, and dried overnight under an Infrared lamp.

The H/D exchange between D$_2$ and ethane was carried out on a CatLab station (Hiden, U.K.) equipped with a mass spectrometer. Specifically, approximately 20 mg of sample was loaded into quartz wool in a quart tube and treated under an H$_2$ atmosphere at 600 °C for 1 h, then cooled to 40 °C. Afterward, the gas flow was switched into a gas flow by mixing 16 mL·min^{-1} of D$_2$ with·1 mL min^{-1} of ethane. Subsequently, the temperature was ramped up to 600 °C at 10 °C·min^{-1}, while the outlet gas was monitored by a mass spectrometer.

The coke species on the spent catalysts were detected by Raman spectroscopy on a LabRAM HR800 spectrograph with a wavelength of 325 nm. In addition, thermogravimetric analysis (TGA) was performed on a Mettler-Toledo TGA/DSC-1 thermal analyzer to quantify the mass of coke species within the used catalysts. Approximately 5 mg of the used catalyst was loaded in the crucible and heated from 30 to 900 °C with a ramping rate of 10 °C·min^{-1} in flowing air (50 mL·min^{-1}). The mass of the sample was continuously recorded throughout the entire process.

Fourier transform infrared (FTIR) spectra of catalysts were recorded on a VERTEX70 spectrometer (Bruker, Germany). The background spectrum was obtained at room temperature under a vacuum before loading the sample. Then, about 30 mg of catalyst was pressed into a self-supporting thin flake with a diameter of 13 mm and loaded into the FTIR cell. Subsequently, the sample was pretreated at 400 °C under vacuum conditions for 2 h to ensure that the water absorbed on the surface of the sample was removed completely. After that, the infrared spectra of the −OH stretching region were recorded under vacuum and room temperature conditions.

X-ray photoelectron spectroscopy (XPS) analysis was performed on the Physical Electronics Company Quantum-2000 Scanning ESCA Microprobe system by using monochromic Al Kα radiation. First, the sample was reduced at 600 °C in H$_2$ for 1 h and then transferred into a sample chamber under oxygen-free conditions in the glovebox. The analytical chamber was maintained below 10^{-10} Pa during data acquisition. The C 1s peak (284.8 eV) of adventitious carbon was used to calibrate the binding energies.

Extended X-ray absorption fine structure (EXAFS) and X-ray absorption near-edge structure (XANES) at the Pt L-edge were measured at the BL11B beamline of the Shanghai Synchrotron Radiation Facility (SSRF). The double crystal Si(111) monochromator was used. Before testing, all of the samples were reduced at 600 °C in H_2 for 1 h and transferred to the glovebox, where the samples were prepared and sealed with Kapton tape. To obtain high-quality data, all of the catalyst samples were pressed into uniform disks with ~6 mm diameter and 2 absorption lengths. Background subtraction was performed using a spline to minimize the non-EXAFS features below 0.1 nm in the Fourier transform, using k^3-weighted data. Multiple scans were collected to ensure spectral reproducibility and a good signal-to-noise ratio. The value of E_0 for the Pt foil (11564 eV) was used for energy alignment. All of the XAS data was analyzed by ATHENA and ARTEMIS software.

The CO adsorption infrared (CO-IR) spectra were conducted on VERTEX 70v spectrometer equipment (Bruker, Germany) with an MCT detector acquiring at 4 cm^{-1} resolution at room temperature. Approximately 30 mg of the catalyst was pressed into a self-supporting thin flake with a diameter of 13 mm and loaded into the cell. Subsequently, the sample was pretreated with hydrogen flow at 600 °C for 2 h to ensure that the Pt clusters were completely reduced. The sample was exposed to a continuous flow of 5% CO/He for 30 min and then flushed with He for CO desorption, while the infrared spectrum was continuously recorded.

Textural properties of Pt-MFI catalysts were analyzed by N_2 physical adsorption−desorption experiments on a Micromeritics ASAP 2020. The surface area and pore distributions were determined by Brunauer−Emmett−Teller (BET) and Barrett−Joyner−Halenda (BJH) methods, respectively. Pore volume was analyzed by the t-plot method at P/P_0 = 0.99.

^{29}Si NMR analysis was conducted on a 600 MHz Bruker Avance III spectrometer operating at a Larmor resonance frequency of 119.11 MHz. A single pulse sequence with a $\pi/4$ pulse length of 2.0 μs and a recycle delay of 20 s was used to acquire ^{29}Si MAS NMR spectra at a sample-spinning frequency of 8 kHz, using Kaoline as the chemical shift reference.

The dispersion of Pt in Pt-MFI catalysts was estimated by CO pulse adsorption on an Altamira AMI-300 equipment. Approximately 100−200 mg of catalysts were reduced in the sample cell under 50 mL·min^{-1} H_2 flow at 600 °C for 1 h, followed by purging under flowing helium (50 mL·min^{-1}) at 615 °C for 30 min. After the mixture was cooled to room temperature, a mixture of 5% CO/95% He (250 μL) was pulsed into the cell for 15−25 consecutive pulses. CO adsorption was continuously monitored to determine the amount of adsorbed CO, assuming a Pt/CO stoichiometry of 1:1. Pt dispersion (D) was calculated using the following equation:

$$D\ (\%) = \frac{VM_{Pt}}{m_{cat} \cdot \omega_{Pt} \cdot V_m} \times 100$$

where V is the CO adsorption capacity (mL), M_{Pt} is the molecular weight of Pt (g/mol), m_{cat} is the mass of the catalyst (g), ω_{Pt} is the mass fraction of Pt in the catalyst, and V_m is the molar volume of gas under standard conditions (22,414 mL·mol^{-1}).

Catalytic Evaluation

The catalytic evaluations were conducted in a fixed-bed reactor (internal diameter = 6 mm) equipped with a K-type thermocouple and heating elements for temperature control and monitoring under atmospheric pressure using a mixture of N_2 and pentane as feed gas. The catalyst was compressed using a pellet press and sieved to collect particles (60−80 mesh) to mitigate the potential mass transfer effects. The catalyst (50−200 mg, diluted with quartz sand in a 1:4 mass ratio) was loaded onto quartz wool inside the quartz tube and reduced in a H_2 atmosphere at 600 °C for 1 h. The fixed bed was then cooled to the required reaction temperature, and the feed was switched to N_2 and pentane, depending on the desired WHSV. Reaction products (pentene, pentadiene, cycloolefins, low-carbon hydrocarbons, etc.) were detected and analyzed online by Agilent 7890B gas chromatography equipped with a flame ionization detector (FID) and a PONA

capillary column. Pentane conversion (X_{pent}) and product selectivity (S_{pro}) were calculated as follows:

$$X_{pent}\ (\%) = \frac{[pentane]_{in} - [pentane]_{out}}{[pentane]_{in}} \times 100$$

$$S_{pro}\ (\%) = \frac{[HC]_{out}}{[pentane]_{in} - [pentane]_{out}} \times 100$$

where $[pentane]_{in}$ and $[pentane]_{out}$ are the concentrations of pentane in the inlet and outlet gas, respectively, and $[HC]_{out}$ represents the concentration of different products in the outlet gas.

■ ASSOCIATED CONTENT

ⓈI Supporting Information

The Supporting Information is available free of charge at https://pubs.acs.org/doi/10.1021/jacsau.4c00949.

Experimental details, chemical compositions of the metal-zeolite materials, electron microscopy, and spectroscopy results of the metal-zeolite materials (PDF)

■ AUTHOR INFORMATION

Corresponding Authors

Hongliu Wan − *State Key Laboratory of Coal Conversion, Institute of Coal Chemistry, Chinese Academy of Sciences, Taiyuan 030001, P. R. China; National Energy Center for Coal to Clean Fuels, Synfuels China Technology Co., Ltd., Beijing 101407, P. R. China;* ⓞ orcid.org/0000-0002-9868-4951; Email: wanhongliu@synfuelschina.com.cn

Lichen Liu − *Department of Chemistry and Engineering Research Center of Advanced Rare-Earth Materials of Ministry of Education, Tsinghua University, Beijing 100084, P. R. China;* ⓞ orcid.org/0000-0001-5067-0481; Email: lichenliu@mail.tsinghua.edu.cn

Authors

Nengfeng Gong − *State Key Laboratory of Coal Conversion, Institute of Coal Chemistry, Chinese Academy of Sciences, Taiyuan 030001, P. R. China; National Energy Center for Coal to Clean Fuels, Synfuels China Technology Co., Ltd., Beijing 101407, P. R. China; University of Chinese Academy of Sciences, Beijing 100049, P. R. China*

Runhui Zhou − *Department of Chemistry and Engineering Research Center of Advanced Rare-Earth Materials of Ministry of Education, Tsinghua University, Beijing 100084, P. R. China*

Huaming Hou − *National Energy Center for Coal to Clean Fuels, Synfuels China Technology Co., Ltd., Beijing 101407, P. R. China*

Xiaomeng Dou − *Department of Chemistry and Engineering Research Center of Advanced Rare-Earth Materials of Ministry of Education, Tsinghua University, Beijing 100084, P. R. China*

Jianhong Gong − *Research Institute of Petroleum Processing, SINOPEC, Beijing 100083, P. R. China*

Peng He − *State Key Laboratory of Coal Conversion, Institute of Coal Chemistry, Chinese Academy of Sciences, Taiyuan 030001, P. R. China; National Energy Center for Coal to Clean Fuels, Synfuels China Technology Co., Ltd., Beijing 101407, P. R. China; University of Chinese Academy of Sciences, Beijing 100049, P. R. China;* ⓞ orcid.org/0000-0002-7141-4660

Complete contact information is available at:

https://pubs.acs.org/10.1021/jacsau.4c00949

■ REFERENCES

(1) Liu, L.; Corma, A. Isolated metal atoms and clusters for alkane activation: Translating knowledge from enzymatic and homogeneous to heterogeneous systems. *Chem* 2021, 7, 2347−2384.

(2) Sattler, J. J. H. B.; Ruiz-Martinez, J.; Santillan-Jimenez, E.; Weckhuysen, B. M. Catalytic Dehydrogenation of Light Alkanes on Metals and Metal Oxides. *Chem. Rev.* 2014, 114, 10613−10653.

(3) Li, X.; Pei, C.; Gong, J. Shale gas revolution: Catalytic conversion of C1−C3 light alkanes to value-added chemicals. *Chem* 2021, 7, 1755−1801.

(4) He, S.; Wang, B.; Dai, X.; Sun, C.; Bai, Z.; Wang, X.; Guo, Q. Industrial development of long chain paraffin (n-C100−C130) dehydrogenation catalysts and the deactivation characterization. *Chem. Eng. J.* 2015, 275, 298−304.

(5) Wan, H.; Gong, N.; Liu, L. Solid catalysts for the dehydrogenation of long-chain alkanes: lessons from the dehydrogenation of light alkanes and homogeneous molecular catalysis. *Sci. China Chem.* 2022, 65, 2163−2176.

(6) Liu, L.; Liu, A. Catalysis paves the way to a new era of the petrochemical industry. *Chem* 2024, 10, 1031−1037.

(7) Alabdullah, M. A.; Gomez, A. R.; Vittenet, J.; Bendjeriou-Sedjerari, A.; Xu, W.; Abba, I. A.; Gascon, J. A Viewpoint on the Refinery of the Future: Catalyst and Process Challenges. *ACS Catal.* 2020, 10, 8131−8140.

(8) Wang, X.; Xu, Y. Recent Advances in Catalytic Conversion of C5/C6 Alkanes to Olefins: A Review. *Catal. Surv. Asia* 2022, 26, 245−260.

(9) Griffiths, S.; Sovacool, B. K.; Kim, J.; Bazilian, M.; Uratani, J. M. Decarbonizing the oil refining industry: A systematic review of sociotechnical systems, technological innovations, and policy options. *Energy Res. Soc. Sci.* 2022, 89, No. 102542.

(10) Wang, Y.; Hu, P.; Yang, J.; Zhu, Y.-A.; Chen, D. C−H bond activation in light alkanes: a theoretical perspective. *Chem. Soc. Rev.* 2021, 50, 4299−4358.

(11) Kumar, A.; Bhatti, T. M.; Goldman, A. S. Dehydrogenation of Alkanes and Aliphatic Groups by Pincer-Ligated Metal Complexes. *Chem. Rev.* 2017, 117, 12357−12384.

(12) Chen, W.; Fu, W.; Duan, X.; Chen, B.; Qian, G.; Si, R.; Zhou, X.; Yuan, W.; Chen, D. Taming Electrons in Pt/C Catalysts to Boost the Mesokinetics of Hydrogen Production. *Engineering* 2022, 14, 124−133.

(13) Biswas, S.; Blessent, M. J.; Gordon, B. M.; Zhou, T.; Malakar, S.; Wang, D. Y.; Krogh-Jespersen, K.; Goldman, A. S. Origin of Regioselectivity in the Dehydrogenation of Alkanes by Pincer−Iridium Complexes: A Combined Experimental and Computational Study. *ACS Catal.* 2021, 11, 12038−12051.

(14) Li, X.; Iglesia, E. Pt/[Fe]ZSM-5 modified by Na and Cs cations: an active and selective catalyst for dehydrogenation of n-alkanes to n-alkenes. *Chem. Commun.* 2008, 44, 594−596.

(15) de la Croix, T.; Claes, N.; Eyley, S.; Thielemans, W.; Bals, S.; De Vos, D. Heterogeneous Pt-catalyzed transfer dehydrogenation of long-chain alkanes with ethylene. *Catal. Sci. Technol.* 2023, 13, 7123−7135.

(16) Tao, J.; Li, X.; Yuan, H.; Ma, A.; Wang, J.; Miao, C.; Liu, C. The effect of potassium on the balance of metal−acid site in Pt/Al2O3 catalysts and their n-hexane dehydrogenation performance. *New J. Chem.* 2024, 48, 12412−12422.

(17) Liu, L.; Lopez-Haro, M.; Lopes, C. W.; Li, C.; Concepcion, P.; Simonelli, L.; Calvino, J. J.; Corma, A. Regioselective generation and reactivity control of subnanometric platinum clusters in zeolites for high-temperature catalysis. *Nat. Mater.* 2019, 18, 866−873.

(18) Liu, L.; Lopez-Haro, M.; Calvino, J. J.; Corma, A. Tutorial: structural characterization of isolated metal atoms and subnanometric metal clusters in zeolites. *Nat. Protoc.* 2021, 16, 1871−1906.

(19) Zhang, W.; Wang, H.; Jiang, J.; Sui, Z.; Zhu, Y.; Chen, D.; Zhou, X. Size dependence of Pt catalysts for propane dehydrogenation: from atomically dispersed to nanoparticles. *ACS Catal.* 2020, 10, 12932−12942.

(20) Qi, L.; Babucci, M.; Zhang, Y.; Lund, A.; Liu, L.; Li, J.; Chen, Y.; Hoffman, A. S.; Bare, S. R.; Han, Y.; et al. Propane dehydrogenation catalyzed by isolated Pt atoms in≡SiOZn−OH nests in dealuminated zeolite Beta. *J. Am. Chem. Soc.* 2021, 143, 21364−21378.

(21) Liu, B.; Wang, F.; Dou, X.; Li, P.; Xiang, H.; Yang, Y.; He, P. Co-aromatization of methane and hexane over Pt encapsulated in ZSM-5 zeolite and the electronic effect of K promoters. *Sci. China Chem.* 2024, 67, 1017−1027.

(22) Dou, X.; Li, W.; Zhang, K.; Hou, H.; He, Z.; Zhu, C.; Meira, D. M.; Lopez-Haro, M.; Xia, Z.; He, P.; et al. Size-dependent structural features of subnanometer PtSn catalysts encapsulated in zeolite for alkane dehydrogenation. *ACS Catal.* 2024, 14, 2859−2871.

(23) DeRita, L.; Resasco, J.; Dai, S.; Boubnov, A.; Thang, H. V.; Hoffman, A. S.; Ro, I.; Graham, G. W.; Bare, S. R.; Pacchioni, G.; et al. Structural evolution of atomically dispersed Pt catalysts dictates reactivity. *Nat. Mater.* 2019, 18, 746−751.

(24) de Graaf, J.; van Dillen, A. J.; de Jong, K. P.; Koningsberger, D. C. Preparation of Highly Dispersed Pt Particles in Zeolite Y with a Narrow Particle Size Distribution: Characterization by Hydrogen Chemisorption, TEM, EXAFS Spectroscopy, and Particle Modeling. *J. Catal.* 2001, 203, 307−321.

(25) Kaylor, N.; Davis, R. J. Propane dehydrogenation over supported Pt-Sn nanoparticles. *J. Catal.* 2018, 367, 181−193.

(26) Nakaya, Y.; Xing, F.; Ham, H.; Shimizu, Ki.; Furukawa, S. Doubly decorated platinum−gallium intermetallics as stable catalysts for propane dehydrogenation. *Angew. Chem., Int. Ed.* 2021, 60, 19715−19719.

(27) Kale, M. J.; Christopher, P. Utilizing quantitative in situ FTIR spectroscopy to identify well-coordinated Pt atoms as the active site for CO oxidation on Al2O3-supported Pt catalysts. *ACS Catal.* 2016, 6, 5599−5609.

(28) Ding, K.; Gulec, A.; Johnson, A. M.; Schweitzer, N. M.; Stucky, G. D.; Marks, L. D.; Stair, P. C. Identification of active sites in CO oxidation and water-gas shift over supported Pt catalysts. *Science* 2015, 350, 189−192.

(29) Nakaya, Y.; Hirayama, J.; Yamazoe, S.; Shimizu, K.-i.; Furukawa, S. Single-atom Pt in intermetallics as an ultrastable and selective catalyst for propane dehydrogenation. *Nat. Commun.* 2020, 11, No. 2838.

(30) Rimaz, S.; Chen, L.; Monzón, A.; Kawi, S.; Borgna, A. Enhanced selectivity and stability of Pt-Ge/Al2O3 catalysts by Ca promotion in propane dehydrogenation. *Chem. Eng. J.* 2021, 405, No. 126656.

(31) Gan, T.; Chu, X.; Qi, H.; Zhang, W.; Zou, Y.; Yan, W.; Liu, G. Pt/Al2O3 with ultralow Pt-loading catalyze toluene oxidation: promotional synergistic effect of Pt nanoparticles and Al2O3 support. *Appl. Catal., B* 2019, 257, No. 117943.

(32) Peng, R.; Li, S.; Sun, X.; Ren, Q.; Chen, L.; Fu, M.; Wu, J.; Ye, D. Size effect of Pt nanoparticles on the catalytic oxidation of toluene over Pt/CeO2 catalysts. *Appl. Catal., B* 2018, 220, 462−470.

(33) Burton, A.; Terefenko, E.; Wang, H.; Paccagnini, M.; Sattler, A. Structure-property relationships that influence platinum stability in all-silica or highly siliceous zeolites. *Microporous Mesoporous Mater.* **2023**, *358*, No. 112655.

(34) Panagiotopoulou, P.; Kondarides, D. I. Effects of alkali additives on the physicochemical characteristics and chemisorptive properties of Pt/TiO$_2$ catalysts. *J. Catal.* **2008**, *260*, 141−149.

(35) Fan, J.; Chen, L.; Li, S.; Mou, J.; Zeng, L.; Jiao, Y.; Wang, J.; Chen, Y. Insights into the promotional effect of alkaline earth metals in Pt-based three-way catalysts for NO reduction. *J. Catal.* **2023**, *418*, 90−99.

(36) Wang, Y.; Liu, H.-H.; Wang, S.-Y.; Luo, M.-F.; Lu, J.-Q. Remarkable enhancement of dichloromethane oxidation over potassium-promoted Pt/Al$_2$O$_3$ catalysts. *J. Catal.* **2014**, *311*, 314−324.

(37) Pazmiño, J. H.; Shekhar, M.; Damion Williams, W.; Cem Akatay, M.; Miller, J. T.; Nicholas Delgass, W.; Ribeiro, F. H. Metallic Pt as active sites for the water−gas shift reaction on alkali-promoted supported catalysts. *J. Catal.* **2012**, *286*, 279−286.

(38) Cao, S.; Zhao, Y.; Lee, S.; Yang, S.; Liu, J.; Giannakakis, G.; Li, M.; Ouyang, M.; Wang, D.; Sykes, E. C. H.; Flytzani-Stephanopoulos, M. High-loading single Pt atom sites [Pt-O(OH)x] catalyze the CO PROX reaction with high activity and selectivity at mild conditions. *Sci. Adv.* **2020**, *6*, No. eaba3809.

(39) Zhao, X.; Zeng, S.; Zhang, X.; Deng, Q.; Li, X.; Yu, W.; Zhu, K.; Xu, S.; Liu, J.; Han, L. Generating assembled MFI nanocrystals with reduced b-axis through structure-directing agent exchange induced recrystallization. *Angew. Chem.* **2021**, *133*, 14078−14087.

(40) Dubray, F.; Moldovan, S.; Kouvatas, C.; Grand, J.; Aquino, C.; Barrier, N.; Gilson, J.-P.; Nesterenko, N.; Minoux, D.; Mintova, S. Direct evidence for single molybdenum atoms incorporated in the framework of MFI zeolite nanocrystals. *J. Am. Chem. Soc.* **2019**, *141*, 8689−8693.

(41) Fegan, S. G.; Lowe, B. M. Effect of alkalinity on the crystallisation of silicalite-1 precursors. *J. Chem. Soc., Faraday Trans.* **1986**, *82*, 785−799.

(42) Kinrade, S. D.; Pole, D. L. Effect of alkali-metal cations on the chemistry of aqueous silicate solutions. *Inorg. Chem.* **1992**, *31*, 4558−4563.

(43) Shao, Z.; Zhang, S.; Liu, X.; Luo, H.; Huang, C.; Zhou, H.; Wu, Z.; Li, J.; Wang, H.; Sun, Y. Maximizing the synergistic effect between Pt^0 and Pt$^{\delta+}$ in a confined Pt-based catalyst for durable hydrogen production. *Appl. Catal., B* **2022**, *316*, No. 121669.

(44) Zhou, J.; Liu, H.; Xiong, C.; Hu, P.; Wang, H.; Wang, X.; Ji, H. Potassium-promoted Pt−In bimetallic clusters encapsulated in silicalite-1 zeolite for efficient propane dehydrogenation. *Chem. Eng. J.* **2023**, *455*, No. 139794.

(45) Chen, H.; Zhang, K.; Feng, Z.; Chen, L.; Zhang, Y.; Zhang, Q.; Peng, B.; Li, D.; Tian, Y.; Huang, R.; Li, Z. Construction of Pd@K-Silicalite-1 via in situ encapsulation and alkali metal modification for catalytic elimination of formaldehyde at room temperature. *Sep. Purif. Technol.* **2024**, *341*, No. 126889.

(46) Zhu, C.; Li, W.; Chen, T.; He, Z.; Villalobos, E.; Marini, C.; Zhou, J.; Woon Lo, B. T.; Xiao, H.; Liu, L. Boosting the Stability of Subnanometer Pt Catalysts by the Presence of Framework Indium(III) Sites in Zeolite. *Angew. Chem., Int. Ed.* **2024**, *63*, No. e202409784.

(47) Jayaraman, A.; Wijerathne, A.; Mandal, K.; Gounder, R.; Paolucci, C. Thermodynamics and kinetics of interconversion between platinum nanoparticles and cations in zeolites. *J. Catal.* **2024**, *434*, No. 115507.

(48) Felvey, N.; Guo, J.; Rana, R.; Xu, L.; Bare, S. R.; Gates, B. C.; Katz, A.; Kulkarni, A. R.; Runnebaum, R. C.; Kronawitter, C. X. Interconversion of Atomically Dispersed Platinum Cations and Platinum Clusters in Zeolite ZSM-5 and Formation of Platinum gem-Dicarbonyls. *J. Am. Chem. Soc.* **2022**, *144*, 13874−13887.

(49) Chen, W.; Qian, G.; Wan, Y.; Chen, D.; Zhou, X.; Yuan, W.; Duan, X. Mesokinetics as a Tool Bridging the Microscopic-to-Macroscopic Transition to Rationalize Catalyst Design. *Acc. Chem. Res.* **2022**, *55*, 3230−3241.

(50) Mériaudeau, P.; Naccache, C. Dehydrocyclization of Alkanes Over Zeolite-Supported Metal Catalysts: Monofunctional or Bifunctional Route. *Catal. Rev.* **1997**, *39*, 5−48.

(51) Isikgor, F. H.; Becer, C. R. Lignocellulosic biomass: a sustainable platform for the production of bio-based chemicals and polymers. *Polym. Chem.* **2015**, *6*, 4497−4559.

(52) Zhang, K.; Dou, X.; Hou, H.; Zhou, Z.; Lopez-Haro, M.; Meira, D. M.; Liu, P.; He, P.; Liu, L. Generation of Subnanometer Metal Clusters in Silicoaluminate Zeolites as Bifunctional Catalysts. *JACS Au* **2023**, *3*, 3213−3226.

(53) Zhu, J.; Yang, M.-L.; Yu, Y.; Zhu, Y.-A.; Sui, Z.-J.; Zhou, X.-G.; Holmen, A.; Chen, D. Size-Dependent Reaction Mechanism and Kinetics for Propane Dehydrogenation over Pt Catalysts. *ACS Catal.* **2015**, *5*, 6310−6319.

(54) Zhang, Y.; Qi, L.; Leonhardt, B.; Bell, A. T. Mechanism and Kinetics of n-Butane Dehydrogenation to 1,3-Butadiene Catalyzed by Isolated Pt Sites Grafted onto ≡SiOZn−OH Nests in Dealuminated Zeolite Beta. *ACS Catal.* **2022**, *12*, 3333−3345.

(55) Sattler, A.; Paccagnini, M.; Liu, L.; Gomez, E.; Klutse, H.; Burton, A. W.; Corma, A. Assessment of metal-metal interactions and catalytic behavior in platinum-tin bimetallic subnanometric clusters by using reactive characterizations. *J. Catal.* **2021**, *404*, 393−399.

(56) Lee, I.; Delbecq, F.; Morales, R.; Albiter, M. A.; Zaera, F. Tuning selectivity in catalysis by controlling particle shape. *Nat. Mater.* **2009**, *8*, 132−138.

(57) Genest, A.; Silvestre-Albero, J.; Li, W.-Q.; Rösch, N.; Rupprechter, G. The origin of the particle-size-dependent selectivity in 1-butene isomerization and hydrogenation on Pd/Al$_2$O$_3$ catalysts. *Nat. Commun.* **2021**, *12*, No. 6098.